Precision Removal of Uneven Skin Tissue at the Micrometer Level via Focus-Corrected Femtosecond-Laser Ablation

Mingzhou Yuan[1,2,#], Xu He[3,#], Guangtao Huang[1,#], Meifang Yin[1,4], Ilaria Dal' Pra[4], Jinqing He[1], Jie Xiao[1], Dehua He[1],Jun Li[3], Xiaofang Liu[1], Rong Zhong[1], Yuncan Ma[3,], and Jun Wu[1,]**

[1]Department of Burn and Plastic Surgery, Medical Innovation Technology Transformation Center, Shenzhen Second People's Hospital, The First Affiliated Hospital of Shenzhen University, Shenzhen 518035, China.

[2]Guangdong Key Laboratory for Biomedical Measurements and Ultrasound Imaging, National-Regional Key Technology Engineering Laboratory for Medical Ultrasound, School of Biomedical Engineering, Shenzhen University Medical School; Shenzhen 518060, China.

[3]Institute of Fluid Physics, China Academy of Engineering Physics; Mianyang 621900, China.

[4]Department of Surgery, Dentistry, Paediatrics and Gynaecology, University of Verona; Verona 37134, Italy.

Mingzhou Yuan, Xu He, and Guangtao Huang contributed equally to this work.

*Corresponding author.
Department of Burn and Plastic Surgery, Medical Innovation Technology Transformation Center, Shenzhen Second People's Hospital, The First Affiliated Hospital of Shenzhen University, Shenzhen 518035, China. E-mail address: junwupro@126.com (Jun Wu)

Institute of Fluid Physics, China Academy of Engineering Physics; Mianyang 621900, China. E-mail address: mayuncan@caep.cn (Yuncan Ma)

Abstract

Background: From the perspective of aesthetic surgery and regenerative medicine, the precision of surgical instruments is critical for preventing aesthetic complications during procedures such as skin debridement and the removal of unwanted tissues, as well as for better regeneration. Femtosecond lasers (fs-lasers) can achieve micrometer-level tissue removal. However, an uneven skin texture can cause the laser to defocus, leading to iatrogenic injury and hindering clinical application. Overcoming the defocusing tendency of fs-lasers is therefore crucial for their clinical use.

Methods: Our self-developed fs-laser microfabrication platform was used to implement a focus-corrected method based on two-dimensional interpolation for uneven skin surfaces, using different laser powers and velocities for linear, planar, and three-dimensional scanning of porcine skin. Leveraging the identified dose–response relationship, the optimized device and parameters were used for precise tissue ablation in an in vivo rat experiment. The structural integrity and viability of the remaining skin were evaluated histologically.

Results: Our study revealed that focus-corrected fs-laser ablation enabled controllable micrometer-level removal of target skin tissues. The depth of tissue removal was correlated with the fs-laser single-pulse energy. Unlike other laser devices, the scanning velocity did not affect the ablation depth, as the focusing mechanism of the focus-corrected fs-laser restricts ablation beyond the focal point. Appropriate fs-laser parameters for parallel linear scanning enabled tissue removal in various three-dimensional shapes. Increased depth of field, increased single-pulse energy, and faster scanning velocity enabled precise, rapid, and safe ablation of skin tissue in the rat model. Histological and biochemical analyses demonstrated that focus-

corrected fs-laser debridement did not damage the surrounding collagen structure or cell viability of the wound.

Conclusions: We demonstrated that focus-corrected fs-laser ablation enables micron-scale skin removal with minimal collateral damage. By selectively adjusting single-pulse energy for depth-specific ablation and operation at the maximum permissible scanning velocity, this technique enables precise skin removal in the desired shape, offering an innovative and ultrahigh-precision surgical approach for skin as well as other tissues or organ surgery.

Highlights:

1. A focus-corrected femtosecond laser platform was developed for micrometer-precision ablation of uneven skin surfaces with minimal collateral damage.

2. A distinct dose–response relationship was observed in femtosecond laser debridement, where the debriding volume was correlated with the single-pulse energy, whereas the volume of tissue removed remained unaffected by the scanning velocity.

3. Reducing the scanning velocity did not result in deepening ablation, as the focusing mechanism of the femtosecond laser restricts ablation beyond the focal point.

Keywords: precision surgery, debridement, femtosecond laser, skin

1 Background

How to remove unwanted tissue with little damage to surrounding tissues is still a major challenge. In skin surgery, the principal methods for the removal of unwanted tissues include scalpel excision and mechanical debridement [1]. However, owing to the limited precision of these methods, damage to surrounding tissues is unavoidable. One study revealed that surgeons may remove more than 40% of normal tissue unintentionally during necrotic skin debridement, which can be detrimental to the skin healing rate and quality [2,3]. Highly precise techniques are essential for skin tissue debridement, particularly in cosmetically and functionally sensitive regions such as the face. Enhancing the precision of surgical debridement remains a

longstanding challenge in clinical plastic surgery. However, lasers present a promising solution to address this issue.

Since the 1970s, lasers have been used in nonsurgical clinical treatments, with various types of lasers being extensively utilized because of their tissue-specific effects [4]. Lasers facilitate precise tissue ablation via the optimization of key operational parameters and can be integrated with automated systems to minimize human error, making them effective options for skin surgery. Nonetheless, although some studies have documented laser skin debridement, experiments suggest that long-pulse laser surgery can result in extensive coagulative necrosis rather than effective tissue removal [5,6]. This is especially detrimental for skin surgery, as excessive trauma significantly augments the propensity for postoperative scarring, which is particularly critical for aesthetically sensitive areas such as the face [7,8]. The issue with traditional pulsed lasers is that the prolonged pulse duration leads to heat transfer to surrounding tissues via thermal diffusion, resulting in protein denaturation and irreversible damage [4]. In contrast, the femtosecond laser (fs-laser), which has the shortest clinically available pulse duration, minimizes thermal diffusion and collateral damage.

The emergence of fs-laser technology, building on the 1980s breakthroughs in chirped pulse amplification, has led to significant advancements in high-energy laser pulse compression, offering an innovative approach for minimally invasive skin surgery [9]. Fs-laser interactions with materials lead to instantaneous temperature peaks and plasma formation, preventing heat diffusion and enabling ‘cold ablation’ by minimizing the heat-affected zone [10,11]. In the medical field, fs-laser technology, which is currently predominantly used in ophthalmology [12], has been investigated for potential applications in other biomedical fields, including stomatology [13], urology [14], otolaryngology [15], and orthopedics [16]. Studies have shown that it causes minimal collateral tissue damage, which highlights its potential as a precision surgical tool. However, despite the successful application of fs-lasers in diseases of the skin that do not require precise control, such as photodynamic therapy (PDT) [17-19], drug delivery enhancement [20], and skin suturing assistance [21], their use as extremely precise surgical instruments in skin surgery has not yet been achieved. The main reason is the challenges posed by uneven skin surfaces, making it difficult to achieve accurate focus control of the fs-laser during the cutting of skin and removal of necrotic skin. The lack of precise calibration and focusing systems can cause unpredictable skin damage, which in turn hinders the exploration of key fs-laser parameters and their effects in skin surgery. However, such exploration is a prerequisite for the clinical application of fs-lasers in this field.

To address the need for precision in skin surgery, this work integrated a three-axis micrometer-precision displacement stage and galvanometric mirror system to control the relative motion between the fs-laser focus and the uneven skin surface, thus facilitating accurate ablation [22]. This self-developed fs-laser microfabrication platform uses customized software to measure and calibrate the distance between the laser focus and the skin surface. By reconstructing the surface topography through two-dimensional (2D) interpolation and projecting treatment paths onto three-dimensional (3D) skin models, the system achieves precise fs-laser surgery. We conducted ex vivo experiments to investigate the effects of key laser parameters (power, scanning velocity, etc.) on skin tissue, thereby establishing optimized protocols for controlled debridement. The efficacy and safety of these protocols were further validated through in vivo animal studies.

2 Methods

2.1 Skin samples and animal preparation

The in vivo experiments were conducted using freshly excised skin from adult Bama miniature pigs. The skin was scalded upon contact with a metal block at a temperature of 100 ℃. Healthy skin and scalded skin were cut into full-thickness skin pieces, each measuring 2 cm × 1 cm. In addition, in vivo experiments were performed with 8-week-old rats. The rats were anesthetized via intraperitoneal injection of Telazol and xylazine prior to the experiment and then placed on the fs-laser processing platform in a warm, comfortable room for fs-laser surgery. All the animal experiments were approved by the Laboratory Animal Welfare and Ethics Committee of China Resources Group (Shenzhen) Co., Ltd. (Approval No. 202400187).

2.2 Construction of the fs-laser microfabrication platform

The experimental optical path of the self-developed fs-laser microfabrication platform is shown in **Figure 1**. The system consists of an fs-laser generator, a laser beam transmission module, an optical microscope, and a high-precision 3D displacement platform. The fs-laser generator serves as the energy source for machining experiments. Its main parameters are as follows: central wavelength of 1030 nm ± 5 nm, pulse duration of 400 fs, maximum single-pulse energy of 200 μJ, and repetition rate of 200 kHz. The beam transmission module is the basic unit for fs-laser beam transmission and consists of four components: a reflector, a diaphragm, an attenuator, and a mechanical shutter. The reflector is used to adjust the laser beam's direction, the diaphragm ensures beam collimation, the attenuator controls the laser power, and the electronically controlled shutter regulates the laser's on/off state. An optical

microscope is essential for laser beam focusing and online monitoring. The object lens is primarily used to concentrate the fs-laser beam. The object lens, in conjunction with the coaxial CCD camera, facilitates real-time monitoring of fs-laser processing. A high-precision 3D displacement platform is the essential element governing the accurate movement of the skin being treated. The main parameters are as follows: stroke X×Y×Z=100 mm×100 mm×50 mm, absolute positioning accuracy ± 0.3 μm, and repeated positioning accuracy ± 0.03 μm. This system can measure the surface profile of the skin, formulate the corresponding scanning path, and ultimately enable precise laser scanning through the motion of the 3D platform.

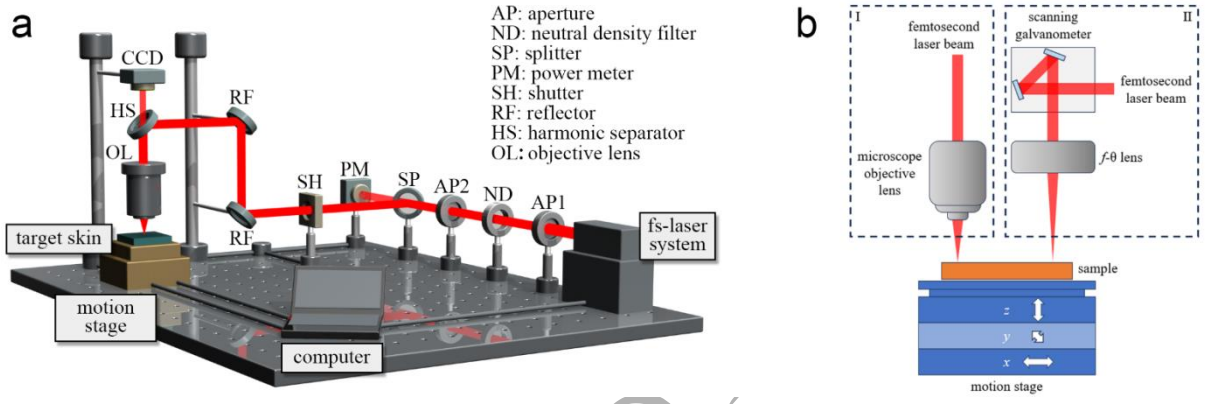

Figure 1. Fs-laser microfabrication platform setup and the integrated focus-corrected scanning structure. **(a)** Structural details of the fs-laser microfabrication platform. **(b)** Focus-corrected scanning structure incorporating laser focusing adjustment and a displacement platform. **I.** The original structure used for in vitro experiments, with a movable displacement platform; **II.** The upgraded structure is suitable for in vivo experiments and is capable of simultaneous laser focus movement and platform movement, enabling precise spatial control during tissue ablation.

2.3 Focus-corrected fs-laser ablation

The surface of skin tissue usually presents various irregularities. Because the latter fluctuations exceed the focal depth range of a laser beam focused by means of a microscope's objective lens, the skin surface cannot be considered an ideal plane during fs-laser skin surgery. In this study, a laser processing method based on two-dimensional interpolation fitting was employed to measure the skin surface and perform focus correction, thereby ensuring that the fs-laser spot was always accurately maintained on the skin surface for scanning movement in skin surgery, as shown in **Figure 2a-d**. The steps of this method are as follows [22]:

I. The original processing path is a series of points in the 2D plane, denoted as $M_i\left(x_i, y_i, z\right)\left(1 \le i \le L, z \equiv z_{\mathrm{M}}\right)$. A rectangular region $\left(x_{\mathrm{a}} \le x \le x_{\mathrm{b}},\ y_{\mathrm{a}} \le y \le y_{\mathrm{b}}\right)$ in the x–y

plane is constructed such that all x_i and y_i of the machining path M_i satisfy $x_a \le x_i \le x_b$ and $y_a \le y_i \le y_b$.

II. The rectangular region is divided in the X and Y directions by equal spacing, and the X and Y coordinates of the division are denoted as $x_1, x_2, \cdots, x_m$ and $y_1, y_2, \cdots, y_n$, respectively.

III. The Z coordinates of points $\left(x_i, y_j\right)\left(1 \le i \le m, 1 \le j \le n\right)$ on the surface of the sample are measured by a laser displacement sensor and included in the matrix $\boldsymbol{Z}_1$:

$$\boldsymbol{Z}_1 = \begin{pmatrix} z_{11} & z_{21} & \cdots & z_{m1} \\ z_{12} & z_{22} & \cdots & z_{m2} \\ \vdots & \vdots & & \vdots \\ z_{1n} & z_{2n} & \cdots & z_{mn} \end{pmatrix}$$

The corresponding $\left(x_i, y_j\right)$ coordinates are included in the matrices $\boldsymbol{X}_1$ and $\boldsymbol{Y}_1$:

$$\boldsymbol{X}_1 = \begin{pmatrix} x_1 & x_2 & \cdots & x_m \\ x_1 & x_2 & \cdots & x_m \\ \vdots & \vdots & & \vdots \\ x_1 & x_2 & \cdots & x_m \end{pmatrix}$$

$$\boldsymbol{Y}_1 = \begin{pmatrix} y_1 & y_1 & \cdots & y_1 \\ y_2 & y_2 & \cdots & y_2 \\ \vdots & \vdots & & \vdots \\ y_n & y_n & \cdots & y_n \end{pmatrix}$$

IV. Some intermediate points $P_{ij}\left(\frac{x_i + x_{i+1}}{2}, \frac{y_j + y_{j+1}}{2}\right)\left(1 \le i \le m-1, 1 \le j \le n-1\right)$ are selected, and the actual z-axis coordinates z_{ij}^{surf} at this point on the sample surface are measured. The matrices $\boldsymbol{X}_1$, $\boldsymbol{Y}_1$, $\boldsymbol{Z}_1$ and the XY coordinates of the intermediate points $P_{ij}\left(x, y\right)$ are imported into MATLAB software, and the two-dimensional interpolation command *z=interp2(X1,Y1,Z1,x,y,'spline')* is executed to calculate the two-dimensional cubic spline interpolation Z coordinates at the position of intermediate points $P_{ij}\left(x, y\right)$ on the surface described by $\boldsymbol{X}_1$, $\boldsymbol{Y}_1$, $\boldsymbol{Z}_1$, which is denoted as z_{ij}^{interp}. The error between the actual Z coordinate and the interpolated Z coordinate is denoted by $\Delta z_{ij} = \left| z_{ij}^{\text{surf}} - z_{ij}^{\text{interp}} \right|$. The processing effect is tested under different defocusing distances, and the absolute value of the maximum defocusing distance that does not affect the processing effect is recorded as $\Delta z_{\max}$. If the maximum value

of Δz_{ij} is less than $\Delta z_{\max}$, proceed to the next step; otherwise, return to step II, increase the number of divisions, and repeat the above steps.

V. The X and Y coordinates of the processing path point $M_i\left(x_i, y_i, z\right)\left(1 \le i \le L, z \equiv z_{\mathrm{M}}\right)$ are included in vectors $\boldsymbol{X}_2$ and $\boldsymbol{Y}_2$, respectively:

$$\boldsymbol{X}_2 = \begin{pmatrix} x_1 & x_2 & \cdots & x_L \end{pmatrix}$$

$$\boldsymbol{Y}_2 = \begin{pmatrix} y_1 & y_2 & \cdots & y_L \end{pmatrix}$$

VI. The above vectors are imported into MATLAB software, and the two-dimensional interpolation command Z2=interp2(X1,Y1,Z1,X2,Y2,'spline') is executed to calculate the two-dimensional cubic spline interpolation Z coordinates corresponding to the XY coordinates of the machining path point $M_i\left(x_i, y_i, z\right)$ on the surface described by $\boldsymbol{X}_1$, $\boldsymbol{Y}_1$, $\boldsymbol{Z}_1$, which is denoted as $\boldsymbol{Z}_2$:

$$\boldsymbol{Z}_2 = \begin{pmatrix} z_1 & z_2 & \cdots & z_L \end{pmatrix}$$

VII. The original processing path is replaced with $M'_i\left(x_i, y_i, z_i\right)\left(1 \le i \le L\right)$, and skin ablation is performed.

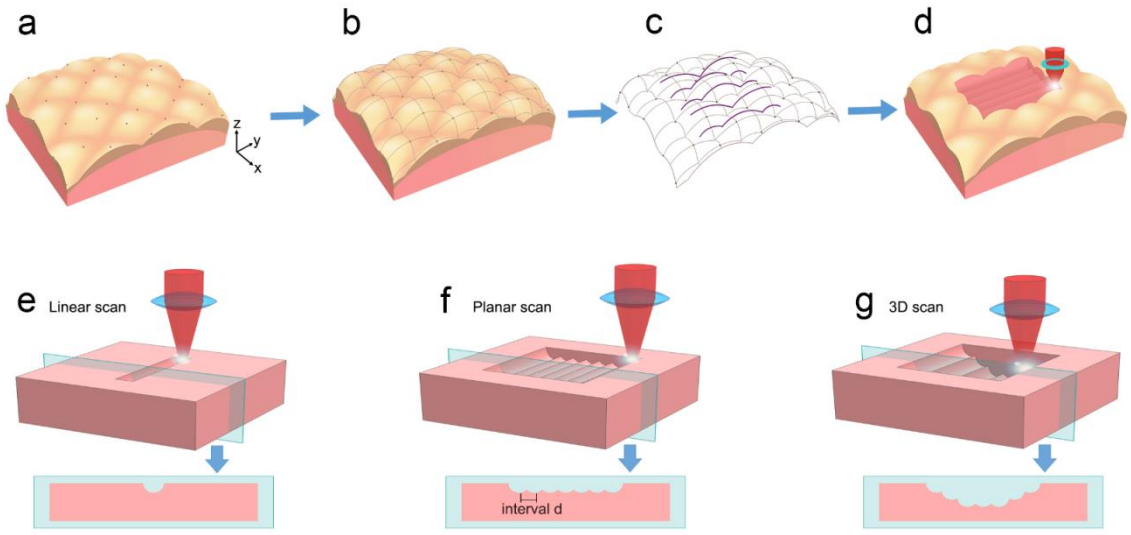

Figure 2. Focus-corrected technology and skin surgery with laser scanning. **(a)** Measuring the height of the sampled points. **(b)** Two-dimensional interpolation fitting. **(c)** Calibrating the laser path via the fitting data. **(d)** Laser skin surgery procedure. **(e)** Linear scan design diagram. **(f)** Planar scan design diagram. **(g)** Three-dimensional scan design diagram.

2.4 In vitro laser scanning protocols

2.4.1 Linear scanning

Following the resolution of the focusing issue with fs-lasers, the dose–effect relationship between different power and scanning velocity settings and the size of the ablated area was investigated. To facilitate the identification and measurement of the ablated area's cross-sectional size under the microscope, the laser scanning path was designed as a straight line. The laser lens was focused on the surface of the skin and scanned over a distance of 5000 μm **(Figure 2e)**. Various laser parameters were applied, comprising power levels of 500 mW, 1000 mW, 1500 mW, and 2000 mW, alongside scanning velocities of 100 μm/s, 200 μm/s, 400 μm/s, 800 μm/s, and 1600 μm/s.

2.4.2 Planar scanning

(I) Line intervals: To investigate the optimal line intervals for achieving a smooth base during planar scanning at different power settings, various line intervals were explored within each power group. Five parallel lines 2000 μm in length were scanned on the skin surface, separated by 2.5 μm intervals, to create a planar debridement **(Figure 2f)**. Similarly, intervals of 5 μm, 7.5 μm, 10 μm, 12.5 μm, 15 μm, 17.5 μm, and 20 μm were employed to perform different kinds of planar debridement. The effects of varying intervals on the depth of debridement and the flatness of the ablation zone were observed.

(II) Line repetitions: Prior investigations have shown that a smooth base can be achieved via a power of 1000 mW and a line interval of 10 μm. To determine whether increasing repetition would lead to an uncontrollable deepening of the ablation zone, we evaluated the ablation zones of different repetition settings during planar scanning. Following the scanning of a line, the laser lens was laterally moved by 10 μm and then refocused, and the scan was reiterated to achieve planar debridement. In the latter step, the depth variations within the ablation areas corresponding to scan tracks 1, 3, 6, and 8 were quantitatively analyzed.

2.4.3 Three-dimensional scanning

Using one of the optimal parameter combinations (power: 1000 mW, scanning velocity: 800 μm/s, line interval: 10 μm) identified in the preceding experiments, the safety and effectiveness of generating the intended three-dimensional ablation zone through planar scanning were validated. With these parameters, nine tracks were scanned on the skin surface to obtain the first-layer plane. The scanning focus was subsequently adjusted to the bottom of this plane, and six additional tracks were scanned to obtain the second-layer plane. This process was repeated, with the scanning focus adjusted again to the bottom of the second-layer plane, and two more tracks were scanned to obtain the third-layer plane **(Figure 2g)**.

2.5 In vivo laser scanning protocols

On the basis of the parameters and patterns obtained from ex vivo experiments, we optimized the fs-laser microfabrication platform to verify the safety and effectiveness of focus-corrected fs-laser ablation for debridement in vivo. The upgraded platform, equipped with a galvanometer scanning microscope, was operated at 1000 mW, 200 kHz, and 2000 mm/s. The rats were anesthetized and placed on the fs-laser processing platform. The skin was affixed with adhesive tape to secure the rats in position, preventing movement due to respiratory motion and exposing only the surgical area. After focusing and recognizing the rat's skin, fs-laser scanning was initiated with focus correction. The laser lens was moved 10 μm, and the process was repeated to complete planar debridement.

2.5.1 One-layer scanning

The scanning length was set to 5000 μm, with 250 repetitions, resulting in a debridement area of 5000 μm × 2500 μm. To accomplish debridement for deep partial thickness burns and ensure that the ablation zone penetrates a deeper dermal layer, the scanning procedure was repeated 10 times.

2.5.2 Two-layer scanning

For the first layer, the scanning length was set to 5000 μm, and scanning was repeated 250 times, which means that the debridement area was set to 5000 μm × 2500 μm. For the second layer, linear scanning was repeated 100 times, which means that the debridement area was set to 5000 μm × 1000 μm. The scanning process for every layer was repeated 10 times.

2.5.3 Three-layer scanning

For the first layer, the scanning length was set to 8000 μm, and linear scanning was repeated 800 times, which means that the debridement area was set to 8000 μm × 8000 μm. For the second layer, linear scanning was repeated 500 times, which means that the debridement area was set to 8000 μm × 5000 μm. For the third layer, linear scanning was repeated 200 times, which means that the debridement area was set to 8000 μm × 2000 μm. The scanning process for every layer was repeated 10 times.

2.6 Tissue imaging and histological examination

2.6.1 Photography and optical coherence tomography

The laser-treated skin samples were examined under a stereomicroscope (*NSZ-606, Nanjing Jiangnan Novel Optics, China*) to document through photography any tissue loss or charring on the skin surface. An optical coherence tomography system (*OCT-1310, Shenzhen*

Shengqiang Technology, China) was utilized to detect the surface contour of the skin postprocessing.

2.6.2 Hematoxylin and eosin (H&E) staining and Masson's trichrome staining

Following fixation of the skin samples in formalin and embedding in paraffin, the tissue samples were meticulously sliced to acquire cross-sectional sections of the ablation zone, ensuring that the distances between the sampled cross-sections were at least 200 μm. Subsequently, 5 μm sections were meticulously prepared and manually stained with H&E and Masson's trichrome.

2.6.3 Lactate dehydrogenase (LDH) staining

LDH staining was employed to evaluate cell viability in situ [23]. In the in vivo experiment, rat skin was sampled immediately after surgery. To preserve tissue viability, the samples were promptly positioned on dry ice. The tissues were then subjected to cryosectioning, with each section having a thickness of 8 μm. The cryostat sections were air-dried at ambient temperature for 2 hours, followed by two washes with PBS, each lasting 5 minutes. The sections were incubated with a freshly prepared LDH solution (*G2360, Beijing Solarbio Science & Technology, China*) that had been thoroughly filtered to remove any impurities for 4 hours at 37 °C. After being washed twice in phosphate-buffered saline, the tissues were counterstained with aqueous eosin (*Changde BKMAM Biotechnology, China*).

2.7 Statistical analysis

This study employed a blinded methodology, wherein individuals responsible for measuring the size of the ablation zone and those performing statistical analyses were not informed of the study group allocation or parameter settings prior to the commencement of the research. The data were analyzed via the SPSS 22.0 statistical software package. The data are expressed as the means ± SDs unless otherwise stated. The depths of the ablation zones across each group were analyzed via one-way analysis of variance (ANOVA) with Tukey's post hoc test (more than two groups). $P < 0.05$ was regarded as statistically significant.

3 Results

3.1 Effect of focus-corrected laser implementation

Optical coherence tomography-three-dimensional (OCT-3D) imaging revealed numerous wrinkles on the skin surface **(Figure 3a)**. When the fs-laser scanning focus was not correctly adjusted and only the average focal length was used to scan the skin surface, an irregular shape of the gasification area was obtained. H&E staining revealed that the surrounding tissue was

fused and necrotic **(Figures 3b and 3c)**. Once the laser processing method based on 2D interpolation fitting was used for fs-laser skin scanning, regular ablation lines were observed on the skin surface **(Figure 3d)**. H&E staining revealed that the fs-laser achieved skin tissue ablation with no obvious visible damage to the surrounding cells or collagen **(Figure 3e)**.

3.2 Range of safety parameters for fs-laser surgery

The results revealed that a considerable degree of carbonization occurred in the skin tissue when the scanning velocity was set to 100 μm/s or 200 μm/s at 2000 mW and 100 μm/s at 1500 mW **(Figure 3f)**. When carbonization occurred along the scanning path, the depth of the ablation zone significantly increased. The carbonized area progressively decreased as the output power decreased and the scanning velocity increased. Using high power and low scanning velocity, both H&E staining and Masson's trichrome staining revealed nuclear condensation and collagen fiber fusion around the gasification area after fs-laser scanning **(Figures 3g and 3h)**. Nevertheless, by reducing the laser power and increasing the scanning velocity, fs-laser scanning generated sharply defined ablation zones on the skin surface without causing cell necrosis or collagen degeneration at the zone margins **(Figures 3i and 3j)**.

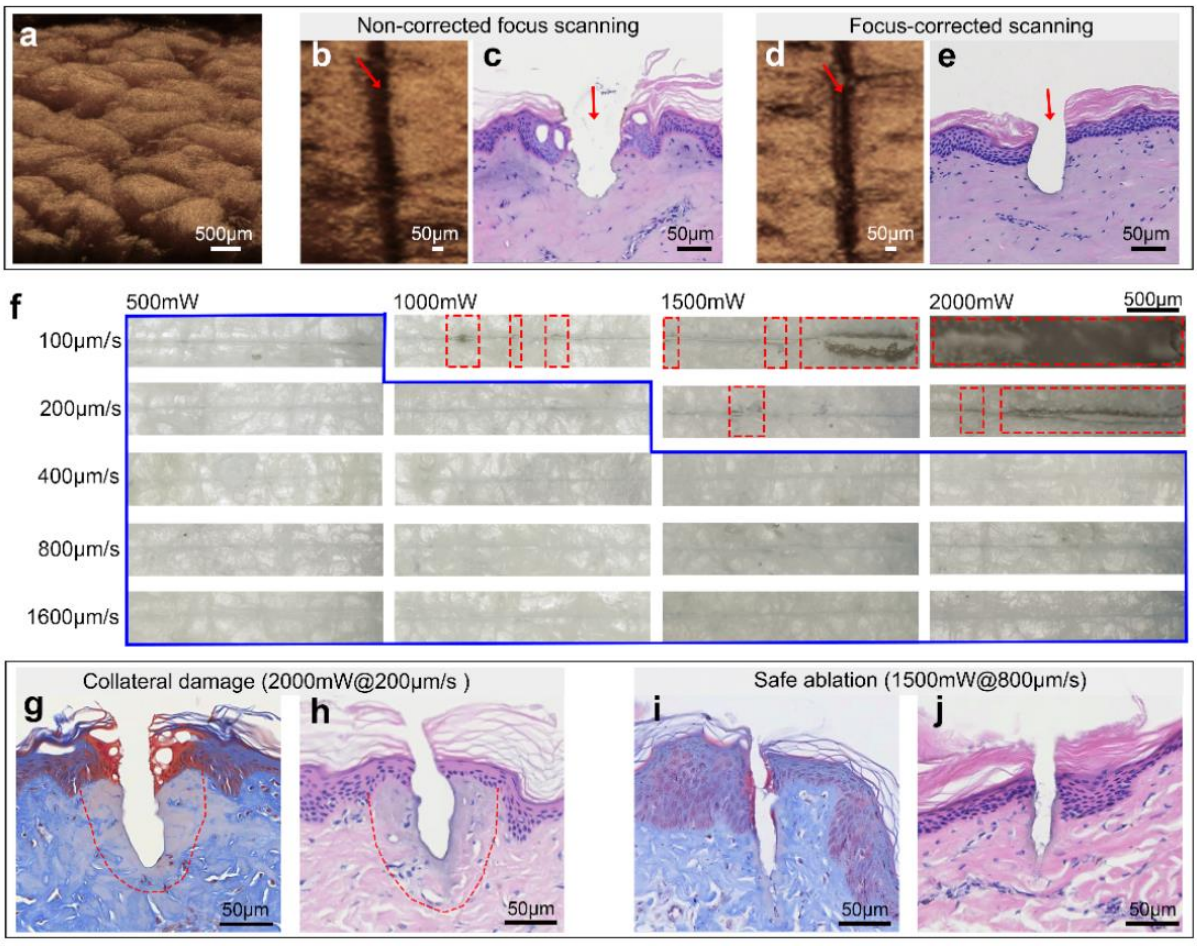

Figure 3. Exploration of the safety parameter ranges for skin surgery. **(a)** OCT-3D imaging of normal skin. **(b)** OCT-3D imaging after noncorrected focus fs-laser linear scanning of the skin surface; **(c)** H&E-stained tissue sections of the ablation zone cross-section after laser scanning. **(d)** OCT-3D imaging after focus-corrected laser scanning and **(e)** the corresponding H&E staining results. The red arrows indicate the scanning path of the fs-laser. **(f)** Appearance of the skin scanning results at different power levels and scanning velocities. The red boxes indicate areas with visible carbonization; the blue boxes indicate conditions without visible carbonization. **(g)** Masson's trichrome staining results showing collagen damage. **(h)** H&E staining results of laser collateral damage. The red dashed lines delineate the area of tissue damage. **(i)** Masson's trichrome staining results of collagen ablation without collateral tissue damage. **(j)** H&E staining results after ablation without collateral tissue damage. Scale bars: a, f: 500 μm; b-e, g-j: 50 μm.

3.3 Dose–response analysis of the Fs-laser parameters

3.3.1 Effects of power and velocity on the skin ablation width

By utilizing safe parameters, fs-laser scanning produced sharp and noncarbonized ablation zones on the skin surface **(Figures 4a and 4b)**. Under the same power conditions, slower scanning velocities did not cause significantly wider ablation zones. With the same scanning velocity, the width of the ablation zone increased with increasing power but not in direct proportion. For example, when the power was doubled from 500 mW to 1000 mW, the width of the ablation zone increased by approximately 32% **(Figure 4c)**.

3.3.2 Effects of power on the skin ablation depth

In the cross-sectional view, following fs-laser scanning of the skin, a sharply bounded ablation zone was observed, exhibiting a semielliptical shape, being broad at the surface and tapering at its deeper region **(Figures 4d and 4e)**. The depth of the ablation zone created by a 500 mW fs-laser scan was approximately 30 μm, which was sufficient to penetrate the stratum corneum and reach the superficial layer of the epidermis. The stratum corneum adjacent to the laser's trajectory had a relatively high density, whereas the epidermis beneath the fs-laser's trajectory showed no obvious morphological changes. At the same scanning velocity, as the laser power increased, the ablation zone became significantly deeper. With the same laser scanning parameters, no significant differences in the depth of the ablation zone were detected between normal skin and partially scalded skin **(Figure 4f)**.

When the output power did not exceed 1500 mW, the surrounding cells remained intact after most of the epidermis had been vaporized. When the power was increased to 2000 mW, the

depth of the ablation zone exceeded 130 μm, reaching the superficial dermis. However, at this level of high power, tissue damage was observable at the periphery of the ablation zone **(Figure 4d4)**.

3.3.3 Effects of velocity on the skin ablation depth

At an output power of 1000 mW, variations in the fs-laser scanning velocity did not significantly influence the depth of the ablation zone **(Figure 4g)**. The ablation zone was notably larger than that observed at other velocities under the same power conditions during carbonization **(Figures 3f and 4c)**. Except when obvious carbonization occurred, the depth of the ablation zone was related to the fs-laser output power, whereas the scanning velocities were irrelevant **(Figures 4f and 4h)**. When a higher output power of the fs-laser was used and the scanning velocity was increased proportionally, the depth and width of the ablation zone continued to increase **(Figure 4i)**. This finding indicates that the size of the ablation zone is primarily determined by the single-pulse energy of the fs-laser rather than by the energy density, which differs from traditional lasers.

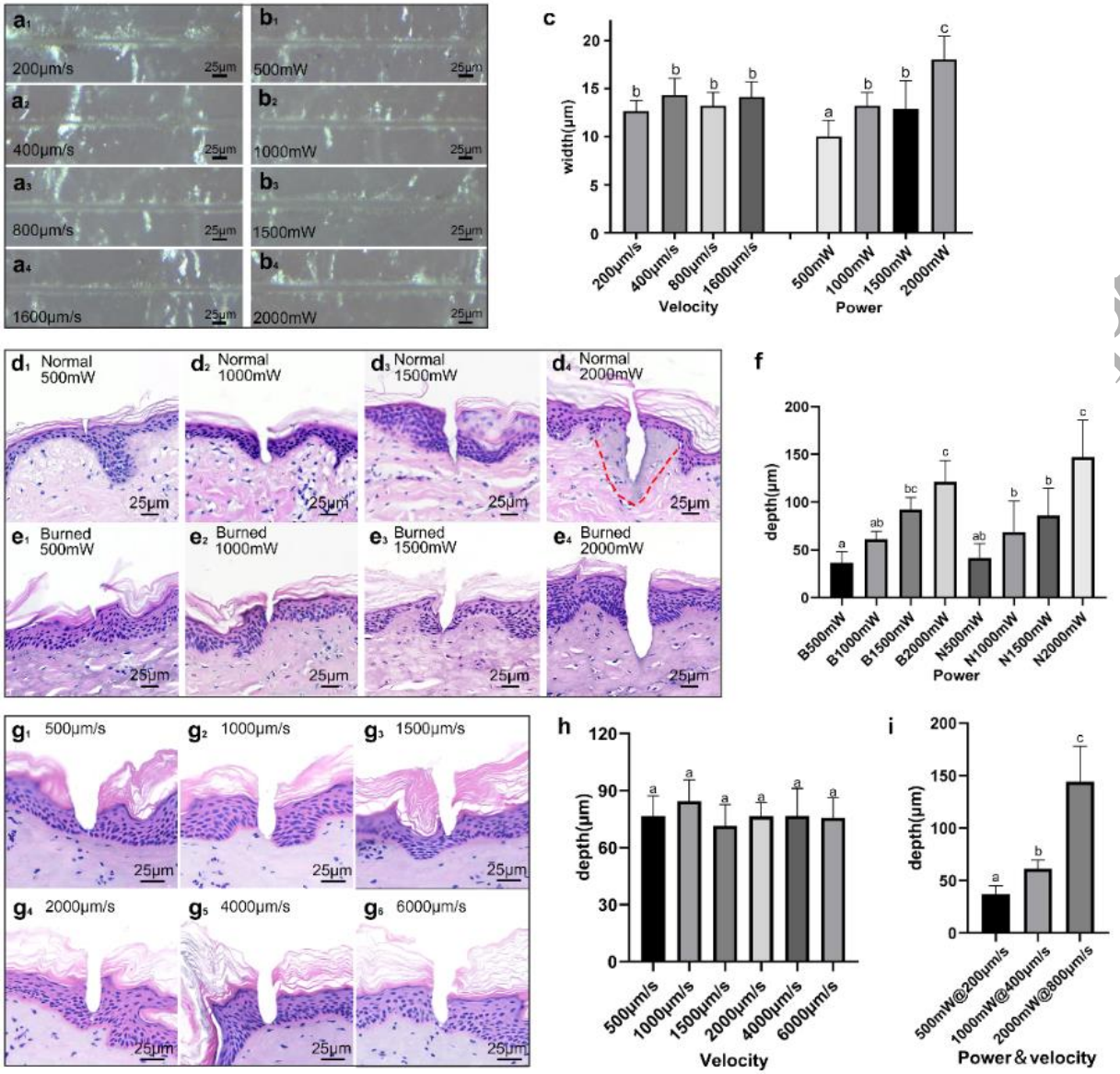

Figure 4. Linear scanning. **(a)** Ablation zone appearance of the skin scanning results under different scanning velocities. **(b)** Ablation zone appearance of the skin scanning results at different powers. **(c)** Width of the ablation zone caused by different scanning velocities at a power of 1000 mW and by different power levels at a velocity of 800 μm/s. **(d)** Cross-sectional histopathological images of normal skin. The red dashed lines indicate tissue damage. **(e)** Cross-sectional histopathological images of burned skin. **(f)** Histograms showing the ablation depths according to the laser power. **(g)** Cross-sectional histopathological images produced at different scanning velocities. **(h)** Histograms showing the ablation depths according to the scanning velocity. **(i)** Histograms showing ablation depths at the same energy density but with different power levels. Different lowercase letters above columns indicate significant differences at $P < 0.05$. Scale bar: 25 μm.

3.4 Controllable clearance of specific shapes

3.4.1 Planar clearance

Line intervals: With velocities of 800 μm/s and powers of 500 mW, 750 mW, 1000 mW, and 1250 mW, the optimal laser scanning line intervals were 5 μm, 7.5 μm, 10 μm, and 15 μm, respectively **(Figures 5a$_2$, 5b$_2$, 5c$_2$, and 5d$_2$)**. When the interval between laser scanning lines was not significantly larger than the aforementioned optimal range, the residual tissue between each pair of lines appeared less clearly. However, when the interval exceeded this range, a smooth base could not be achieved. When the interval was smaller than the optimal line interval, the base of the ablation zone exhibited a flat profile, but its depth was significantly greater than that produced by a single scan. Nonetheless, excessively small line intervals led to ablation areas of unpredictable sizes **(Figures 5a$_1$, 5b$_1$, 5c$_1$, and 5d$_1$)**, making it unsuitable to achieve greater tissue removal depth by reducing the line intervals.

Line repetitions: The ablation depth in the 3-scan group was significantly greater than that in the 1-scan group, but the ablation depth was similar among the 3-, 6-, and 8-scan groups **(Figures 5g and 5f)**. This finding indicates that tissue removal using parallel linear scanning to form various shapes was both controllable and stable.

3.4.2 Three-dimensional clearance

The measured depth of the first-layer ablation zone was the combined result of the thickness of both the stratum corneum and the epidermis/dermis. Therefore, the depth of the first layer ablation zone was greater than that of the second layer and the third layer **(Figures 5h and 5i)**. When the tissues to be vaporized were entirely in the dermis, the depths of the second- and third-layer ablation zones did not significantly differ. This suggests that the presence of the stratum corneum might result in deeper ablation of the first tissue layer by approximately 20 μm than during the removal of deeper tissues, which should be factored into the debridement plan. On the basis of the above parameters and features, cuboid-shaped skin tissue ablation was accomplished through parallel linear stacking and cylindrically shaped ablation via concentric circular arc stacking **(Figures 5j and 5k)**.

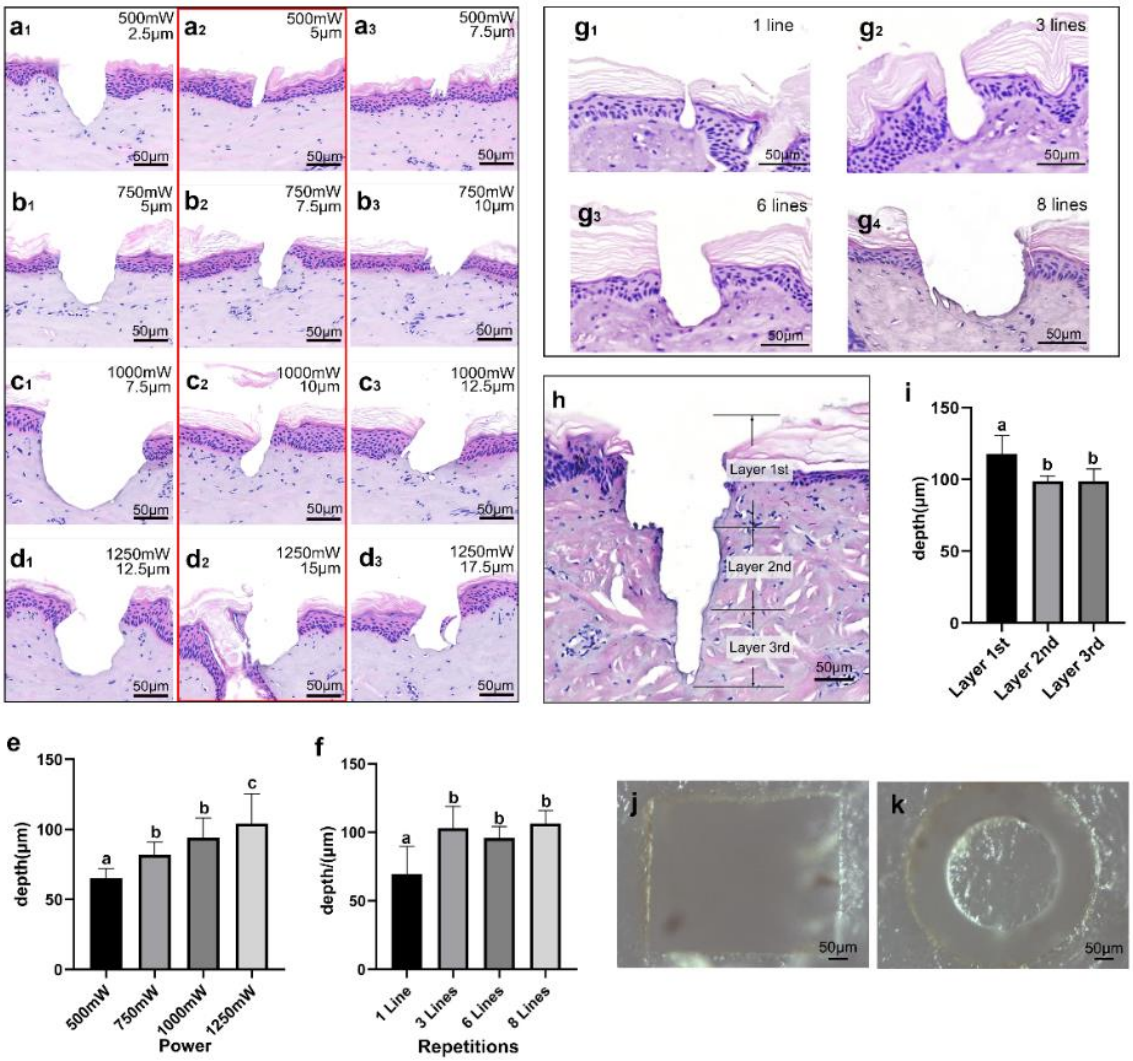

Figure 5. Planar scanning and 3D scanning. **(a-d)** Cross-sectional histopathological images of planar scans at different intervals. **(e)** Histograms showing the depths of the ablation areas after different power outputs of planar laser scanning. **(f)** Histograms showing the depths of the ablation areas after different repetitions of planar laser scanning. **(g)** Cross-sectional histopathological pictures of the ablation zone after linear laser scanning with different repetitions. **(h)** H&E-stained cross-sectional skin section showing the results of 9 lines for layer 1, 6 lines for layer 2, and 2 lines for layer 3. **(i)** Depth of each 3D scanning layer. The effects of straight path **(j)** and circular path scanning **(k)**. Different lowercase letters above columns indicate significant differences at $P < 0.05$. Scale bar: 50 μm.

3.5 In vivo skin response following fs-laser surgery

3.5.1 Removal of specific-shaped skin via multilayer scanning

Fs-laser scanning debridement of the dorsal skin of rats enabled the controlled and precise removal of single-layer, double-layer, and triple-layer skin tissues with varying morphologies. After fs-laser debridement, the boundaries of the debrided area were clearly demarcated and

sharply delineated, and the size of the area matched the predefined rectangular region **(Figure 6a)**. With a set scanning velocity of 2,000,000 μm/s and a line interval of 10 μm, the times required for the removal of the first, second, and third layers of triple-layer tissue were 3.2 seconds, 2.0 seconds, and 0.8 seconds, respectively.

3.5.2 Histological evaluation after fs-laser surgery

Hematoxylin and eosin staining revealed a localized loss of skin tissue in the femtosecond laser-ablated area, characterized by sharply demarcated boundaries. The residual collagen fibers at the base of the ablation zone exhibited staining intensity and density comparable to those of the adjacent normal dermis. Furthermore, at the interface between the ablated and unablated areas, the architecture of epidermal cells, fibroblasts, and hair follicle structures remained intact, without evidence of either necrosis or degeneration **(Figures 6b$_1$-6b$_3$)**.

3.5.3 Cell viability after fs-laser surgery

Lactate dehydrogenase serves as a marker for active cells, and eosin counterstaining is used to delineate tissue morphology. The ablated area exhibited epidermal removal, resulting in the exposure of the underlying tissue and cells. The uppermost layer of cells retained a considerable amount of blue precipitate **(Figures 6c$_1$-6c$_3$)**, and the staining intensity was similar to that of the adjacent unablated dermal region. This finding indicates that the fs-laser at this energy value successfully ablated the tissue while preserving the viability of the basal cells.

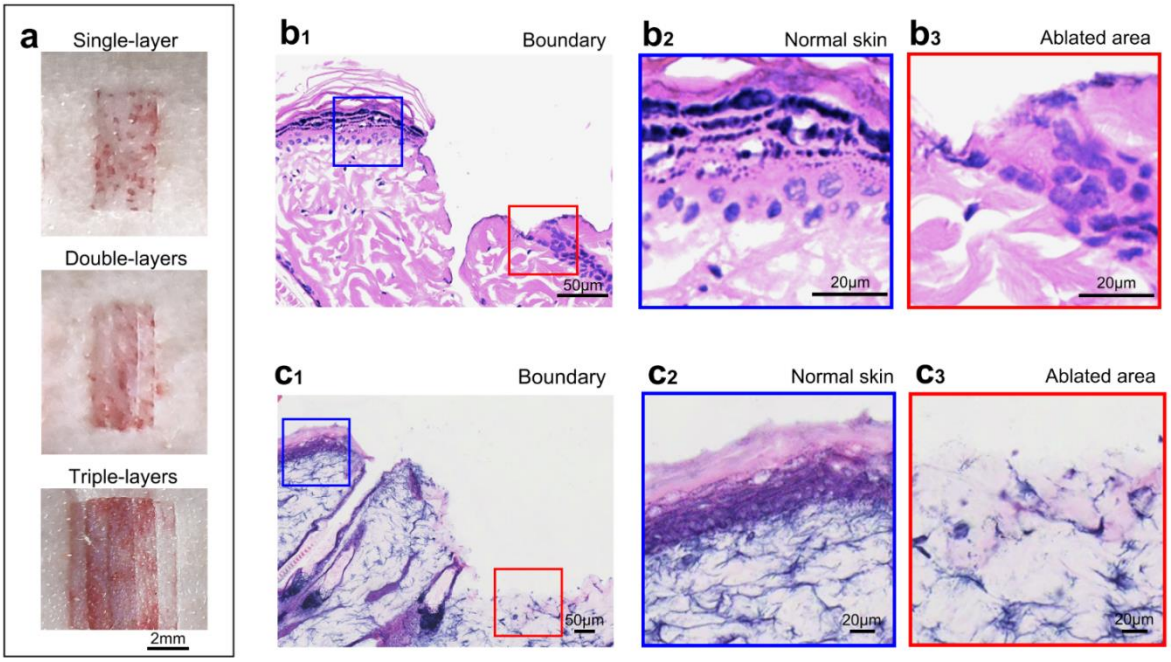

Figure 6. Histological evaluation of rat skin after fs-laser surgery. **(a)** Appearance of rat dorsal skin after fs-laser ablation via single-, double-, and triple-layer scanning. **(b)** Hematoxylin and eosin staining of skin tissue sections at the boundary between the ablated and unablated areas

(b_1). High-magnification images of normal skin (b_2, blue box) and the ablated area (b_3, red box) are shown. **(c)** Costaining with lactate dehydrogenase and eosin shows tissue viability at the boundary between ablated and unablated areas (c_1). Representative high-magnification images show the normal area (c_2, blue box) and the ablated area (c_3, red box). Scale bars: a: 2 mm; b_1, c_1: 50 μm; b_2, b_3, c_2, c_3: 20 μm.

4 Discussion

This study demonstrated that focus-corrected fs-laser ablation could overcome the defocus of uneven skin surfaces and generate an ablation zone while preserving adjacent skin tissue from collateral damage. Our further findings indicated that the depth of the ablation zone correlates with the laser power output but remains unaffected by the scanning velocity, demonstrating a distinct divergence from that of conventional lasers. Using this principle, a galvanometer-based scanning microscope was employed to increase the scanning velocity and successfully achieved the efficient removal of skin tissues as needed. Moreover, this approach did not adversely affect the viability of skin cells in the in vivo debridement experiment. The evidence presented here indicates that fs-laser ablation can achieve micron-level precision, with surgical accuracy reaching the cellular scale.

The skin is a structurally complex organ characterized by microscale variations, such as folds, furrows, and hair follicles, which pose significant challenges for achieving precise fs-laser focus during dynamic scanning [3]. Although fs-lasers are well known for inducing nonlinear and highly precise tissue ablation [12], our results showed that defocused irradiation, particularly under excessive pulse energy and insufficient scanning velocity, can lead to linear energy absorption and thermal injury. Specifically, when the laser becomes defocused and is delivered outside the intended site, the energy density fails to reach the vaporization threshold. Instead, residual energy is absorbed via linear photothermal processes, increasing local temperatures and causing carbonization [24]. Once a carbonized layer forms, its increased optical absorbance and decreased scattering further enhance energy deposition, aggravating thermal damage [25]. This feedback loop is a major barrier to achieving collateral-free fs-laser surgery on the skin. Similarly, even after successful ablation in focus, a slow scanning velocity can result in repeated out-of-focus exposure of adjacent tissue. Under high pulse energy conditions, thermal energy can accumulate over an extremely short duration, further exacerbating the risk of injury. To address these issues, we developed a focus correction strategy incorporating preoperative multipoint focusing, two-dimensional interpolation, topographic skin surface reconstruction, and individualized path projection. By combining

lower single-pulse energies with higher scanning velocities, this approach effectively avoids thermal damage. To our knowledge, this is the first study to propose a practical operational framework for safe and effective fs-laser debridement. This optimized approach lays a promising foundation for further quantitative studies on the fs-laser dose–response relationship in skin debridement.

Further characterization of the dose–response relationship revealed that fs-laser ablation behaves differently from conventional lasers in terms of tissue removal. In traditional continuous-wave or long-pulse laser scanning, the vaporization zone typically expands with increasing power. Conversely, higher scanning velocities reduce local energy deposition per unit area, thus decreasing tissue removal [26]. However, fs-laser ablation does not follow this pattern. While a higher fs-laser pulse energy increases the ablation depth, slower scanning does not reduce the depth of the ablation zone. Instead, excessively slow scanning leads to thermal accumulation and carbonization. This phenomenon aligns with the principles of the 'effective spot' concept in precision micromachining, wherein higher pulse power enlarges the effective spot diameter and increases the volume of affected tissue [27,28]. This explains why high-energy fs-laser pulses result in deeper and more extensive ablation zones. In our experiments, when the fs-laser operated at 200 kHz with a 20 μm spot size and at a scanning speed of 1000 μm/s, each point along the ablation trajectory received up to 4000 overlapping pulses. Under these parameters, the vaporization region reached the lower boundary of the effective spot, whereas the tissue beyond this focal volume remained unaffected. These findings establish a clear dose–effect relationship between the output power and ablation depth, independent of the scanning velocity. This fundamental divergence underscores the unique interaction mechanisms of fs-lasers compared with those of conventional lasers. Importantly, this study elucidates the dose–response characteristics required for safe and efficient fs-laser debridement, providing critical guidance for future clinical translation through both parameter refinement and hardware optimization.

Building on our insights into the dose–response relationship and operational performance, we identified key avenues for enhancing the fs-laser ablation platform. Central to this effort was the integration of a high-velocity galvanometer-based scanning microscope, which increased the scanning velocity to 2,000,000 μm/s, allowing ablation to be completed prior to exudate accumulation, thereby preserving optical clarity and procedural efficiency. In parallel, we implemented an elliptical spot-focusing design that extended the effective focal depth, enabling consistent energy delivery across microscale surface irregularities such as skin wrinkles. This configuration mitigated defocus-induced thermal injury and reduced the

complexity of intraoperative focus adjustment. Collectively, these technological refinements position the focus-corrected fs-laser platform as a promising tool for a range of surgical applications, including precise wound debridement, micron-resolution incisions of skin appendages, and enhanced transdermal drug delivery via selective stratum corneum ablation.

Despite the promising outcomes, several aspects of this study warrant further refinement to enable clinical translation. First, our experiments were conducted with a 1030 nm fiber fs-laser; further investigations are needed to determine the optimal wavelength for skin ablation. If alternative wavelengths are considered, the dose–response relationship must be re-evaluated accordingly. Second, while porcine skin and rat models provide valuable preclinical insights, the structural disparities in stratum corneum thickness and skin appendage density between these models and human skin underscore the need for validation using human tissues to refine operational power thresholds. Third, although effective in scalded wound debridement, the generalizability to other skin conditions, such as neoplastic lesions, remains unverified and merits dedicated exploration. Fourth, as the current system remains a proof-of-concept prototype, further engineering is necessary for clinical readiness. This includes developing skin fixation accessories, streamlining the software interface, and optimizing laser parameters to increase procedural efficiency, stability, and usability in clinical debridement settings. Finally, to fully leverage the benefits of micrometer-scale laser debridement, it is essential to assess the depth of necrotic skin accurately. A noninvasive imaging technique based on near-infrared spectroscopy, capable of micron-level assessment of necrosis depth, was developed by our team [29]. Future studies integrating spectral detection with fs-laser debridement technology may represent transformative advances in skin surgery.

5 Conclusions

In summary, this study demonstrates that focus-corrected fs-laser ablation has a distinct and quantifiable dose–response relationship that fundamentally differs from that of conventional laser technologies. Specifically, debridement depth correlates with single-pulse energy, whereas reductions in scanning velocity do not result in increased tissue loss. Through optimized power output and high-speed scanning, micron-level precise ablation of skin tissue on uneven surfaces can be achieved without collateral thermal damage. This tunable parameter space enables quantitative control over surgical outcomes, underscoring the substantial potential of fs-laser technology in advancing the safety, precision, and efficacy of skin surgery.

Author contributions

Mingzhou Yuan, Xu He, Guangtao Huang, Yuncan Ma, and Jun Wu conceived and designed the study; Mingzhou Yuan, Xu He, and Guangtao Huang drafted the manuscript; Mingzhou Yuan, Meifang Yin, Jinqing He, Jie Xiao, and Dehua He performed the biological experiments; Xu He, Yuncan Ma, and Jun Li were responsible for the fs-laser ablation system; Mingzhou Yuan, Xu He, Yuncan Ma, Ilaria Dal' Pra, Guangtao Huang, Xiaofang Liu, and Rong Zhong conducted the data analysis and interpretation; Yuncan Ma and Jun Wu supervised the project and reviewed and revised the final manuscript. All the authors read and approved the final version of the manuscript.

Abbreviations

fs-laser: femtosecond laser; PDT: photodynamic therapy; 2D: two-dimensional; 3D: three-dimensional; CCD: charge-coupled device; H&E: hematoxylin and eosin; LDH: lactate dehydrogenase; ANOVA: one-way analysis of variance; OCT: optical coherence tomography.

Ethics approval and consent to participate

This study was approved by the Laboratory Animal Welfare and Ethics Committee of China Resources Group (Shenzhen) Co., Ltd. (Approval No. 202400187) and was conducted in accordance with the NIH Guide for the Care and Use of Laboratory Animals.

Conflict of interest

All the authors declare that they have no conflicts of interest.

Funding

This study received funding from the Shenzhen High-level Hospital Construction Fund (4004006), the Sanming Project of Medicine in Shenzhen (SZSM202111020), the National Natural Science Foundation of China (82172214, 11704357), the National Key Research and Development Program (2022YFC2403101), and the Key Laboratory Fund for Shock Wave Physics and Detonation Physics (2021JCJQLB05707).

Data availability

The datasets generated and analyzed during the current study are available from the corresponding author upon reasonable request.

References

1. Kwa KAA, Goei H, Breederveld RS, Middelkoop E, van der Vlies CH, van Baar ME. A systematic review on surgical and nonsurgical debridement techniques of burn wounds. *Journal of Plastic, Reconstructive & Aesthetic Surgery* 2019;**72**:1752-1762.
2. Gurfinkel R, Rosenberg L, Cohen S, Cohen A, Barezovsky A, Cagnano E, et al. Histological assessment of tangentially excised burn eschars. *Can J Plast Surg* 2010;**18**:e33-e36.
3. Dal Prà I, Chiarini A, De Santis D, Nocini R, Chang S, Armato U. The quest for the perfect healing of human skin wounds: Promising models. *Regenesis Repair Rehabilitation* 2025;**1**:66-79.
4. Vogel A, Venugopalan V. Mechanisms of Pulsed Laser Ablation of Biological Tissues. *Chem Rev* 2003;**103**:577-644.
5. Doizi S, Germain T, Panthier F, Compérat E, Traxer O, Berthe L. Comparison of Holmium:YAG and Thulium Fiber lasers on soft tissue : an ex vivo study. *J Endourol* 2022;**36**:251-258.
6. Weisberg NK, Kuo T, Torkian B, Reinisch L, Ellis DL. Optimizing fluence and debridement effects on cutaneous resurfacing carbon dioxide laser surgery. *Archives of dermatology (1960)* 1998;**134**:1223-1228.
7. Chopra K, Calva D, Sosin M, Tadisina KK, Banda A, De La Cruz C, et al. A Comprehensive Examination of Topographic Thickness of Skin in the Human Face. *Aesthet Surg J* 2015;**35**:1007-1013.
8. Dunkin CSJ, Pleat JM, Gillespie PH, Tyler MPH, Roberts AHN, McGrouther DA. Scarring Occurs at a Critical Depth of Skin Injury: Precise Measurement in a Graduated Dermal Scratch in Human Volunteers. *Plast Reconstr Surg* 2007;**119**:1722-1732.
9. Strickland D, Mourou G. Compression of amplified chirped optical pulses. *Opt Commun* 1985;**56**:447-449.
10. He S, Yu J, Hu M. Femtosecond Laser High Precision Fabrication for Novel Applications. *Curr Nanosci* 2016;**12**:676-684.
11. Kononenko VV, Gololobov VM, Komlenok MS, Konov VI. Nonlinear photooxidation of diamond surface exposed to femtosecond laser pulses. *Laser Phys Lett* 2015;**12**:96-101.
12. Latz C, Asshauer T, Rathjen C, Mirshahi A. Femtosecond-Laser Assisted Surgery of the Eye: Overview and Impact of the Low-Energy Concept. *Micromachines-basel* 2021;**12**:122.
13. Loganathan S, Santhanakrishnan S, Bathe R, Arunachalam M. Physiochemical characteristics: A robust tool to overcome teeth heterogeneity on predicting laser ablation

profile. *Journal of Biomedical Materials Research Part B: Applied Biomaterials* 2021;**109**:486-495.

14. Teichman JMH. Femtosecond laser lithotripsy: feasibility and ablation mechanism. *J Biomed Opt* 2010;**15**:028001.
15. Andrus L, Mau T, Ben-Yakar A. Scattering properties and femtosecond laser ablation thresholds of human and canine vocal folds at 776-nm wavelength. *J Biomed Opt* 2019;**24**:085005.
16. Gemini L, Al-Bourgol S, Machinet G, Bakkali A, Faucon M, Kling R. Ablation of Bone Tissue by Femtosecond Laser: A Path to High-Resolution Bone Surgery. *Materials* 2021;**14**:2429.
17. Hu B, Zhao X, Lu Y, Zhu Y, He H. A transient photoactivation of epidermal stem cells by femtosecond laser promotes skin wound healing. *J Biophotonics* 2022;**15**:e202200217.
18. Nicolodelli G, Angarita DPR, Inada NM, Tirapelli LF, Bagnato VS. Effect of photodynamic therapy on the skin using the ultrashort laser ablation. *J Biophotonics* 2014;**7**:631-637.
19. Santos MOD, Latrive A, De Castro PAA, De Rossi W, Zorn TMT, Samad RE, et al. Multimodal evaluation of ultra-short laser pulses treatment for skin burn injuries. *Biomed Opt Express* 2017;**8**:1575-1588.
20. Garvie Cook H, Stone JM, Yu F, Guy RH, Gordeev SN. Femtosecond pulsed laser ablation to enhance drug delivery across the skin. *J Biophotonics* 2016;**9**:144-154.
21. Jia M, Huang J, Chen Y, JinchengLi, Wang K. Experimental study on the effect of scanning path on skin tissue properties of femtosecond laser welding. *J Biophotonics* 2023;**16**:e202300205.
22. He X, Ma Y, Li J, Yuan M, Yin M, Meng L, et al. Method and Application of Femtosecond Laser Processing on Non-Flat Surfaces. *Laser Optoelectron P* 2023;**60**:1714009.
23. Gibson ALF, Shatadal S. A simple and improved method to determine cell viability in burn-injured tissue. *J Surg Res* 2017;**215**:83-87.
24. Zhang X, Chen X, Chen T, Ma G, Zhang W, Huang L. Influence of Pulse Energy and Defocus Amount on the Mechanism and Surface Characteristics of Femtosecond Laser Polishing of SiC Ceramics. *Micromachines-basel* 2022;**13**:1118.
25. Gill RK, Smith ZJ, Lee C, Wachsmann Hogiu S. The effects of laser repetition rate on femtosecond laser ablation of dry bone: a thermal and LIBS study. *J Biophotonics* 2016;**9**:171-180.

26. Dmitriev AK, Konovalov AN, Kortunov VN, Ulyanov VA. Evaporation Peculiarities of Soft Biological Tissues in the Process of Automated 2D-Scanning of CO_2 Laser Radiation. *Journal of Biomedical Photonics & Engineering* 2024;**10**:040307.
27. Lin Z, Hong M. Femtosecond Laser Precision Engineering: From Micron, Submicron, to Nanoscale. *Ultrafast Science* 2021;**2021**:9783514.
28. Wang B, Wang X, Zheng H, Lam YC. Thermal effect of femtosecond laser polystyrene processing. *Optics & Laser Technology* 2019;**117**:244-250.
29. Yin M, Li Y, Luo Y, Yuan M, Armato U, Prà ID, et al. A novel method for objectively, rapidly and accurately evaluating burn depth via near infrared spectroscopy. *Burns Trauma* 2021;**9**:tkab014.